Machine-learning-assisted design of a binary descriptor to decipher electronic and structural effects on sulfur reduction kinetics

Check for updates

Zhiyuan Han[1,3], Runhua Gao[1,3], Tianshuai Wang [2,3], Shengyu Tao[1], Yeyang Jia[1], Zhoujie Lao[1], Mengtian Zhang[1], Jiaqi Zhou[1], Chuang Li[1], Zhihong Piao[1], Xuan Zhang [1] & Guangmin Zhou [1] ✉

The catalytic conversion of lithium polysulfides is a promising way to inhibit the shuttling effect in Li–S batteries. However, the mechanism of such catalytic systems remains unclear, which prevents the rational design of cathode catalysts. Here we propose the machine-learning-assisted design of a binary descriptor for Li-S battery performance composed of a band match (I_{Band}) and a lattice mismatch (I_{Latt}) indexes, which captures the electronic and structural contributions of cathode materials. Among our Ni-based catalysts, $NiSe_2$ exhibits a moderate I_{Band} and the smallest I_{Latt} and is predicted and subsequently verified to improve the sulfur reduction kinetics and cycling stability, even with a high sulfur loading of 15.0 mg cm^{-2} or at low temperature (−20 °C). A pouch cell with $NiSe_2$ delivers a gravimetric specific energy of 402 Wh kg^{-1} under high sulfur loading and lean-electrolyte operation. Such a fundamental understanding of the catalytic activity from electronic and structural aspects offers a rational viewpoint to design Li–S battery catalysts.

Despite the high theoretical capacity (1,675 mAh g^{-1}), cost effectiveness, natural abundance and environmental friendliness of elemental sulfur, the commercialization of lithium−sulfur (Li–S) batteries is still seriously restricted by sluggish reaction kinetics[1,2]. The high activation energy of the conversion from lithium polysulfides (LiPSs) to insoluble Li_2S_2/Li_2S leads to the accumulation of LiPSs and exacerbates the shuttling effect as well as producing severe capacity decay[3]. Catalytic conversion of LiPSs is a crucial approach to enhancing these kinetics[4–6]. Transition-metal-compound (TMC) catalysts, such as metal oxides[7], sulfides[8], nitrides[9] and selenides[10], have often been used to accelerate the sluggish sulfur reduction and improve sulfur utilization. Because of the solid nature of the end charge/discharge products, the catalytic

activity is believed to have a volcano-shaped relationship with LiPS adsorption, as proposed by Zhang and others[11]. Weak adsorption allows LiPSs to diffuse towards the lithium anodes with fast capacity decay, but too strong adsorption suppresses the desorption of Li_2S_2/Li_2S, inducing passivation of the catalysts and reducing the catalytic activity. The strength of the adsorption of LiPSs depends on the electronic coupling between the active sites of the catalysts and adsorbed LiPSs, which is related to the hybridization level of the orbitals. The metal centres of TMCs with partially filled d orbitals are always regarded as active sites[12]. A metal with a higher d-band centre displays a higher LiPS adsorption strength by decreasing the fraction of occupied antibonding states. Many strategies have been proposed, such as alloying[13,14],

[1]Tsinghua-Berkeley Shenzhen Institute & Tsinghua Shenzhen International Graduate School, Tsinghua University, Shenzhen, P. R. China. [2]School of Chemistry and Chemical Engineering, Northwestern Polytechnical University, Xi'an, P. R. China. [3]These authors contributed equally: Zhiyuan Han, Runhua Gao, Tianshuai Wang. ✉e-mail: guangminzhou@sz.tsinghua.edu.cn

defect engineering[15,16] and crystal structure regulation[17,18], to adjust the *d*-band centre relative to the Fermi level to modulate the binding energy for a fast redox reaction.

Although *d*–*p*-orbital hybridization between metal cations and polysulfide anions has been widely studied during analysis of the catalytic mechanism[19–21], the role in the catalytic process of the non-metal anions of TMCs has received less attention. The notable influence of non-metal anions in TMCs towards the adsorption energy to LiPSs can be observed among different metal-based TMCs (Supplementary Fig. 1). Qian and others reported that shifting the *p*-band centres of the anions modulates the interfacial electron-transfer dynamics by controlling their energy gap with transition-metal *d*-band centres[22]. However, the influence on the catalytic process of the widely discovered interactions between the anions of TMCs and Li in lithium (poly)sulfides still lacks systemic understanding[15,16,23]. Moreover, previous works have usually focused mostly on interpreting the electronic states of catalytic systems[15,16,18,20,23–25]. However, the geometric structure of the optimal active sites also influences the catalytic performance. For example, the coordination numbers of the binding atoms at active sites scale with the adsorption energies[26]. Therefore, the bandstructure alone is insufficient to decipher the intrinsic modulation essence of anions towards the sulfur reduction activity of TMC catalysts. Unfortunately, binary descriptors (BDs) for TMCs that simultaneously consider both the electronic and structural properties of sulfur-reduction catalytic systems, and thus have more accurate prediction ability, have never been investigated. These persistent issues have plagued the rational design and activity tuning of catalysts for Li–S batteries.

In this Article we describe the design of a four-step workflow to identify an experimentally validated BD using Ni-based TMCs as a model system. We first conduct a Pearson correlation analysis to search the most relevant features, specifically the band match index (I_{Band}) and lattice mismatch index (I_{Latt}), to describe the adsorption energy and reaction energy barrier from both electronic and structural aspects. Density functional theory (DFT) and experimental testing are then conducted to investigate the contributions of I_{Band} and I_{Latt} to the sulfur reduction kinetics of the TMCs. We find that decreasing the I_{Band} value leads to the enhancement of adsorption, but a too-low I_{Band} can cause passivation of the catalysts. Meanwhile, decreasing I_{Latt} weakened the Li–S bond, facilitating the decomposition of lithium (poly)sulfides on the TMC surfaces. Those TMCs with moderate I_{Band} and low I_{Latt} can improve the conversion of LiPSs and facilitate the decomposition of Li_2S, thus showing the best catalytic activity. We then determine the BD using a genetic algorithm to search coefficient combinations in large parameter spaces and use Monte Carlo simulations to validate the uncertainties. $NiSe_2$ was predicted to be a highly efficient catalyst, as was also confirmed by experiments. Li–S cells with $NiSe_2$ demonstrated the best battery performance when compared with those with different Ni-based TMCs, showing the lowest electrochemical barrier for LiPS reduction/Li_2S oxidation and high specific capacity with ultrahigh loading (15.0 mg cm⁻²). Finally, an ampere hour (Ah)-level Li–S pouch cell with $NiSe_2$ attained a high specific energy of 402 Wh kg⁻¹ at a high areal-sulfur loading of 17.3 mg cm⁻² and an electrolyte/sulfur ratio (E/S) of 4 µl mg⁻¹. The proposed BD reveals the influence of anions in Ni-based TMCs, from electronic and structural aspects, and offers a rational viewpoint from which to analyse LiPS conversion and the design of efficient catalysts. For other similar study paradigms requiring the perspective of electronic and structural effects, the designed BD could be further applied to other TMCs as a universal descriptor.

Results

Development of the electronic and structural descriptor

The first step of the four-step workflow (Fig. 1a) is feature extraction. In the Li–S battery system, the effect of electronic coupling between the catalysts and adsorbed LiPSs, which is related to the hybridization level of orbitals or energy bands, determines their adsorption strength[12]. In our previous work, we found that the *d*–*p*-orbital hybridization between

single-atom metal catalysts (SACs) and sulfur species can be used as a descriptor for understanding the catalytic activity of SACs in Li–S batteries[20]. However, this is not applicable to TMCs, as they include dual centres of metal cations and non-metal anions, which respectively interact with the sulfur and lithium in the LiPS species. The electronic coupling between TMCs and LiPS species includes two hybridizations: *d* orbitals from the cations of TMCs and *p* orbitals from the sulfur of LiPS species, and *p* orbitals from the anions of TMCs and *s* orbitals from the lithium of the LiPS species. Although the *d*–*p* hybridization for metal cations has been studied, the crucial effects of *s*–*p* hybridization on modulating the Li–S chemistry have rarely been investigated because of the difficulty of disentangling the above two effects. Our previous work found that Li–N bonds rather than Ni–S bonds are formed between Li_2S and single-atom Ni catalysts because of the poor *d*–*p* hybridization process, indicating that Ni-based compounds may be a suitable model with which to highlight the impact of *s*–*p* hybridization on the catalytic effect[20]. For multi-electron redox reactions, it is the intermediates of the rate-determining step that determine the catalytic activity. Therefore, taking NiO as an example, the activation energy (E_a) for each step of the LiPS reduction process was first experimentally determined by probing the charge-transfer resistance at the corresponding voltages under various temperatures (Supplementary Figs. 2 and 3)[3]. To stabilize the voltage for a specific conversion step, the cell was discharged to a targeted potential and chronoamperometry was performed until the output current remained constant. Electrochemical impedance spectra (EIS) were then obtained from 2.4 V to 1.9 V in the frequency range from 100 mHz to 100 kHz with an alternating-current amplitude of 5 mV. The charge-transfer resistance at different temperatures was fitted using the simplified-contact Randles equivalent circuit, which revealed a linear relationship between the inverse of absolute temperature and the logarithm of the reciprocal of the charge-transfer resistance. E_a was then derived by following the Arrhenius reaction. The resulting E_a indicates that the conversion of the S_8 molecules to soluble LiPSs is relatively easy. However, the conversion of LiPSs into the ultimate insoluble products is more difficult and is the rate-determining step for Li–S batteries, consistent with previous reports[3]. The obvious overpotential observed in the discharge profiles of the Li–S battery with a high sulfur loading of 3 mg cm⁻² also confirms the most serious kinetic problem for the Li_2S_4 reduction process (Supplementary Fig. 4). Note that the current density (0.1 C) is far from the mass transport-limiting region for typical batteries and thus serves well for the purpose of kinetic studies. To consider the severe shuttle effect, which is primarily related to soluble LiPSs, the electronic structure of the system containing Ni-based TMCs (Ni_3C, Ni_2P, NiO, NiS_2 and $NiSe_2$) and Li_2S_4 was studied to reveal the underlying *s*–*p* hybridization (Fig. 1b). We propose the I_{Band} to describe the band centre relationship between the active sites of Li_2S_4 and TMCs. Different TMCs with various combinations of cations and anions may change the relative strengths of the *d*–*p* and *s*–*p* hybridizations. To enhance the suitability of I_{Band}, we define $I_{Band} = \left| \frac{\varepsilon_p - \varepsilon_d}{\varepsilon_p} \right| + \left| \frac{\varepsilon_s - \varepsilon_p}{\varepsilon_s} \right|$, which considers both the *d*–*p* and *s*–*p* hybridizations simultaneously. $I_{Band}(d$–$p)$, $\left| \frac{\varepsilon_p - \varepsilon_d}{\varepsilon_p} \right|$, is defined by the *p*-band centre position (ε_p) of the sulfur in Li_2S_4 and the *d*-band centre position (ε_d) of the cations (Ni, Fe, Co, Ti, V and so on) in the TMCs. $I_{Band}(s$–$p)$, $\left| \frac{\varepsilon_s - \varepsilon_p}{\varepsilon_s} \right|$, is defined by the *s*-band centre position (ε_s) of the lithium in Li_2S_4 and the ε_p of the anions (C, P, O, S, Se and so on) in TMCs. Here, I_{Band} describes the energy gap between the TMCs and Li_2S_4, and the smaller value suggests a lower energy gap of the band centre, corresponding to higher interfacial electron-transfer dynamics and a stronger interaction between the TMCs and Li_2S_4. The *p*-band centre of non-metal anions of Ni-based TMCs varies among TMCs (0.751 eV for Ni_3C, −0.028 eV for Ni_2P, −1.018 eV for NiO, −2.207 eV for NiS_2 and −1.391 eV for $NiSe_2$; Fig. 1c). From Ni_2P to NiS_2, the I_{Band} increases from 1.374 to 7.663 (Fig. 1d and Supplementary Table 1). LiPS adsorption was further simulated and analysed using DFT (details of the model construction details are
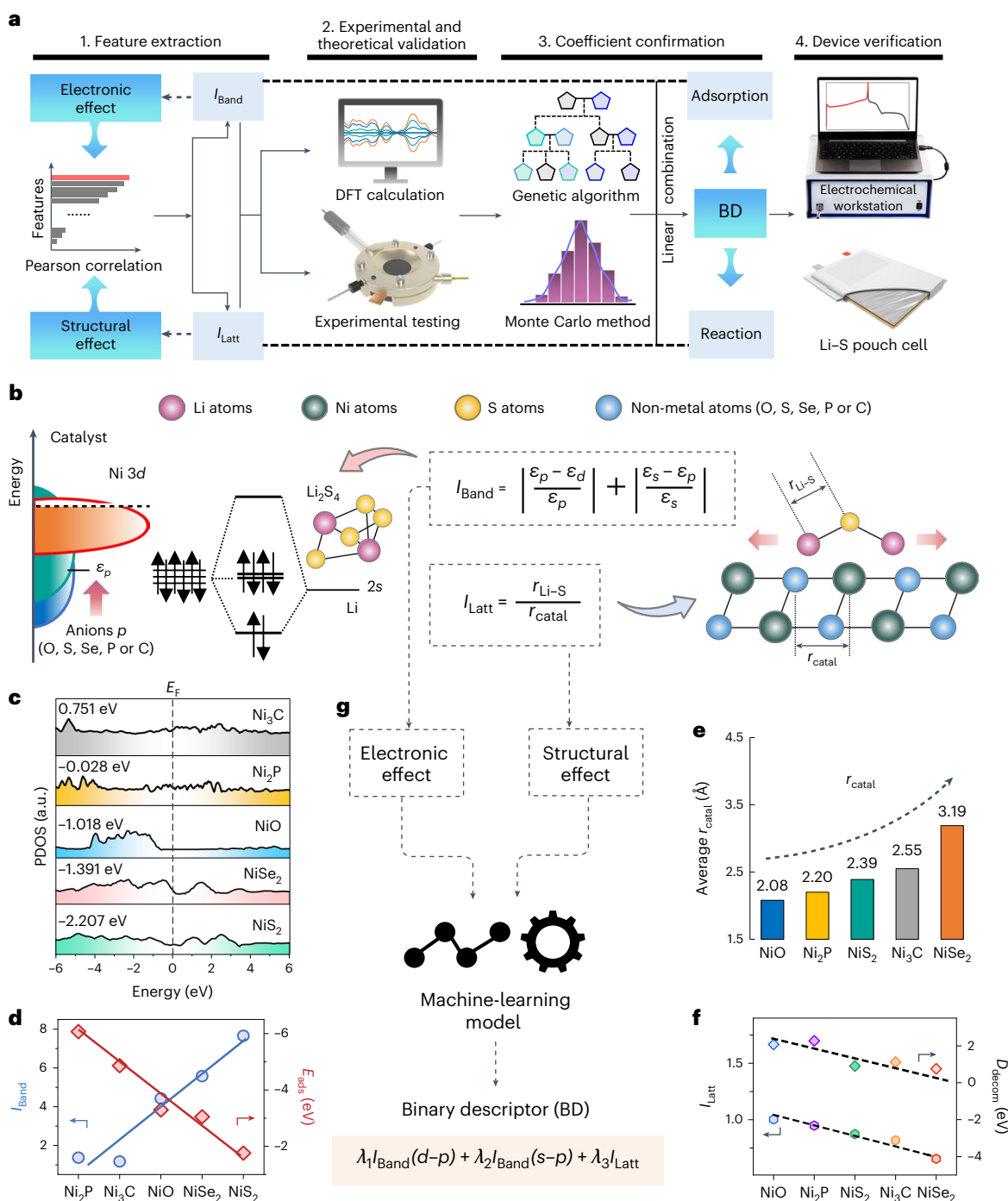
Fig. 1 | Introduction of electronic and structure descriptors. a, The overall workflow diagram, showing the steps of feature extraction, experimental and DFT analysis, coefficient confirmation and device verification. **b**, Development of the electronic descriptor, I_{Band}, and structural descriptor, I_{Latt}, of Ni-based TMCs. Both are dimensionless. **c**, Projected density of states (PDOS) on p orbitals for five Ni-based TMC candidates: Ni_3C, Ni_2P, NiO, $NiSe_2$ and NiS_2. E_F, Fermi energy. Vertical dashed line indicates E_F. **d**, I_{Band} and E_{ads} of various Ni-based TMCs for Li_2S_4. **e**, r_{catal} of various Ni-based TMCs. **f**, Relationship between the decomposition energy barrier (D_{decom}) of adsorbed Li_2S and I_{Latt} of various Ni-based TMCs. **g**, Development of the BD simultaneously considering electronic and structural effects. I_{Band} and I_{Latt} are dimensionless, and hence BD is also dimensionless.

provided in Methods). The adsorption energy between the catalysts and LiPSs is much larger than between the electrolyte solvents and LiPSs (Fig. 1d and Supplementary Figs. 5), indicating that the LiPS molecules tend to interact with the catalysts. Accordingly, to simplify the calculations, complex theoretical models of the solvation structures of LiPSs were not adopted in the kinetic analysis of LiPS conversion on the catalysts with strong anchoring ability. The geometric configurations

of the adsorption models are displayed in Supplementary Figs. 6 and 7. We conducted a Pearson correlation analysis to explore the potential correlation between I_{Band} and the electronic effect, considering various features of the TMCs simultaneously (further information is provided in Supplementary Note 1). The absolute values of the Pearson correlation coefficient, which indicates the relative importance of these features, are presented in descending order in Supplementary Fig. 8. The results

indicate that the I_{Band} of $d-p$ and $s-p$ hybridization have a considerable influence on the adsorption energy. The adsorption energy (E_{ads}) of Ni-based TMCs shows an approximately opposite trend to that of I_{Band} (Fig. 1d), as is also observed for other TMCs (Supplementary Fig. 9 and Supplementary Table 2). According to the relation between adsorption energy and catalytic activity, the medium adsorption capability of LiPSs suggests improved conversion and facilitated desorption[11].

Structural effects resulting from variations in the radii of anions lead to different crystal structures and lattice spacings of TMCs. Given that different thermodynamic and dynamic processes are involved in the oxidation and reduction of sulfur species, delithiation and lithiation are discussed separately here. To represent the difference in lattice spacing between TMCs and lithium (poly)sulfides, we defined a structural descriptor, I_{Latt}, as $\frac{r_{Li-S}}{r_{catal}}$ (Fig. 1b and Supplementary Table 3), where r_{Li-S} and r_{catal} correspond to the lattice spacing of Li–S in lithium (poly) sulfides and average cations–anions in TMCs, respectively. The average lattice spacing of cations–anions is used to take different crystal faces into account. In this way, complicated calculation of the adsorption configuration is avoided and the practicability of I_{Latt} is enhanced. I_{Latt} then connects the geometric structure of optimal active sites with catalytic performance, making it possible to design TMCs by constructing specific active sites. Figure 1e summarizes r_{catal} for Ni-based TMCs, which is seen to range from 2.08 Å for NiO to 3.19 Å for NiSe$_2$. The larger r_{catal} corresponds to lower I_{Latt} (Fig. 1f). Geometric structure analysis was conducted for the system with Li$_2$S or Li$_2$S$_4$ adsorbed on Ni-based TMCs. Taking the delithiation process as an example, Li$_2$S was studied because the oxidation of Li$_2$S is recognized as the most kinetically slow step due to its high E_a[10,20,27]. The obvious overpotential of 62.6 mV at the beginning of the charging profiles, corresponding to the oxidation of Li$_2$S, confirms the serous kinetic problem (Supplementary Fig. 10). In situ NMR has also been used to prove the sluggish oxidation of Li$_2$S (ref. 28). Here, we consider the decomposition process from an intact Li$_2$S molecule into a LiS cluster and a single Li ion (Li$_2$S → LiS + Li$^+$ + e$^-$), corresponding to the Li–S bond breaking (Supplementary Fig. 11). The decomposition energy barrier can be obtained by use of climbing image-nudged elastic band (CI-NEB) methods[29] (Fig. 1f). Pearson correlation analysis indicates that I_{Latt} is the most relevant feature in determining the delithiation energy barrier, in comparison to other factors (Supplementary Fig. 12). The scaling relationship between I_{Latt} and the delithiation energy barrier (Fig. 1f) reveals that a low I_{Latt} decreases the energy barrier for the delithiation process by weakening the Li–S bond in Li$_2$S. For the lithiation process, the scaling relationship between I_{Latt} and the kinetic energy barrier for breaking the S–S bond in Li$_2$S$_4$ indicates that I_{Latt} correlates well with the reaction processes (Supplementary Figs. 13 and 14).

To conclude, based on the constructed electronic and structural descriptor, it is seen that the anions in TMCs can modulate I_{Band} and I_{Latt}. Those TMCs with moderate I_{Band} and low I_{Latt} tend to simultaneously have medium adsorption towards LiPSs and a low reaction energy barrier, thus increasing the catalytic activity. Guided by the above theoretical calculations, we prepared three Ni-based TMCs (NiO, NiS$_2$ and NiSe$_2$) from the same column of the periodic table and tested their catalytic properties. A BD simultaneously considering the electronic and structural effects was further proposed with the genetic algorithm searching coefficient combinations in large parameter spaces and with Monte Carlo simulations validating the uncertainties (Fig. 1g). The dimensionless nature of both I_{Band} and I_{Latt} imparts a corresponding dimensionless quality to the BD.

Electronic descriptor scaling with the adsorption process

To reveal the role of anions, from both electronic and structural aspects, we selected Ni-based TMCs as the model system because nickel has a weak interaction with sulfur and the effect of $s-p$ hybridization on catalytic activity can be highlighted reasonably easily[30–33]. Different anions are coordinated, modifying I_{Band} and I_{Latt}. As the lithium cations of the

various LiPSs mainly interact with the anions in the TMCs and their binding energies are coupled to the p-band centre, the activity of Ni-based TMCs is tuned accordingly. Following this strategy, we synthesized Ni-based TMC (NiO, NiS$_2$ and NiSe$_2$) catalysts. Their preparation and characterization are shown in Supplementary Note 2, Supplementary Figs. 15–23 and Supplementary Table 4. Figure 2a presents the molecular configuration of Li$_2$S$_4$ on the (001) surface of the NiSe$_2$ catalyst. After geometric optimization, two Li atoms of Li$_2$S$_4$ were attached to the surface Se anions, while the S atom was attracted to the Ni cations of the catalyst (other TMCs are shown in Fig. 2b,c). Electron-density difference analysis was then used to uncover the adsorption mechanism (Fig. 2d–f), revealing the relationship of strong adsorption processes and the interfacial charge interaction.

To verify our theoretical predictions and evaluate the relationship between I_{Band} and the adsorption energy of TMCs for LiPSs, UV–vis absorption spectroscopy was used to investigate the adsorption ability of NiO, NiS$_2$ and NiSe$_2$ in a Li$_2$S$_6$ solution when controlling for the same surface area (Fig. 2g). After adsorption for 1.5 h, the intensity of the remaining S$_6^{2-}$ follows the order NiS$_2$ > NiSe$_2$ > NiO. This trend is consistent with visual observations (Fig. 2g, inset), with an orange-coloured Li$_2$S$_6$ solution with NiO turning almost colourless after 1.5 h, whereas that with NiS$_2$ showed only slight decolouring within the same time. The extracted adsorption intensity of Li$_2$S$_6$ and Li$_2$S$_4$ from Fig. 2g shows that NiO has the strongest adsorption ability, and NiS$_2$ has the weakest (Fig. 2h), consistent with the previous predictions based on their electronic structures (Fig. 1d). The TMCs with low I_{Band} decrease the energy gap between the band centres of the TMCs and LiPSs, leading to high adsorption capability. The chemical interaction between the LiPSs and TMCs was investigated by X-ray photoelectron spectroscopy (XPS). The peak assigned to NiO in the O 1s spectra is shifted to a higher binding energy after interacting with Li$_2$S$_6$, suggesting an apparent reduction in the oxygen electron density via electron transfer (Fig. 2i). X-ray diffraction (XRD) and XPS spectra suggest that NiO does not react with the LiPSs (Supplementary Figs. 24 and 25). Their chemical interactions verify that the LiPSs easily passivate NiO with low I_{Band}. However, Ni–S and Ni–Se peaks in the S 2p and Se 2p spectra of NiS$_2$ and NiSe$_2$ (Supplementary Figs. 26 and 27) are barely shifted, indicating a relatively weaker interaction between sulfur or selenium than that with oxygen, which agrees with the predictions based on their I_{Band} values.

According to the volcano trend between catalytic activity and adsorption strength[11], NiSe$_2$, with its medium adsorption capability for LiPSs, prevents passivation of the catalyst surface, and is thus more effective in accelerating the reaction reactivity of LiPSs and suppressing the shuttling effect during cycling. We thus assembled Li–S coin cells with Ni-based TMC catalysts and tested the shuttle current. The cell with NiSe$_2$, with a medium I_{Band}, shows a smaller shuttle current (9.94×10^{-4} mA cm^{-2}) than cells with NiO and NiS$_2$ (Supplementary Fig. 28), indicating that it has the best effect on suppressing the LiPS shuttle. The severe shuttling effect seen for the cell with NiO occurs because of passivation of the catalyst surface. In situ Raman spectroscopy was used to gain insight into the regulation of the shuttle effect by NiSe$_2$. When analysing the diffusion of LiPSs to the lithium anode side, only a few signals corresponding to S$_6^{2-}$ are detected during both the discharge and charge processes for the cathodes with NiSe$_2$ (Fig. 2j,k), demonstrating an effective alleviation of the shuttle effect. In contrast, for cathodes without NiSe$_2$, two intense peaks (153.5 and 281.5 cm^{-1}) attributed to S$_8^{2-}$ are detected at the beginning of the discharge process (Fig. 2l,m). When discharging to 2.066 V, signals of S$_6^{2-}$ and S$_4^{2-}$ + S$_3^{2-}$ are detected, and they remain during the subsequent charging process. Notable signals for S$_6^{2-}$, S$_4^{2-}$ and S$_3^{2-}$ confirm the existence of severe LiPSs shuttling, which is responsible for the capacity loss.

Structural descriptor scaling with the reaction process

Based on the above theoretical analysis, the structural descriptor I_{Latt} determines the dissociation of LiPS through modification of the surface
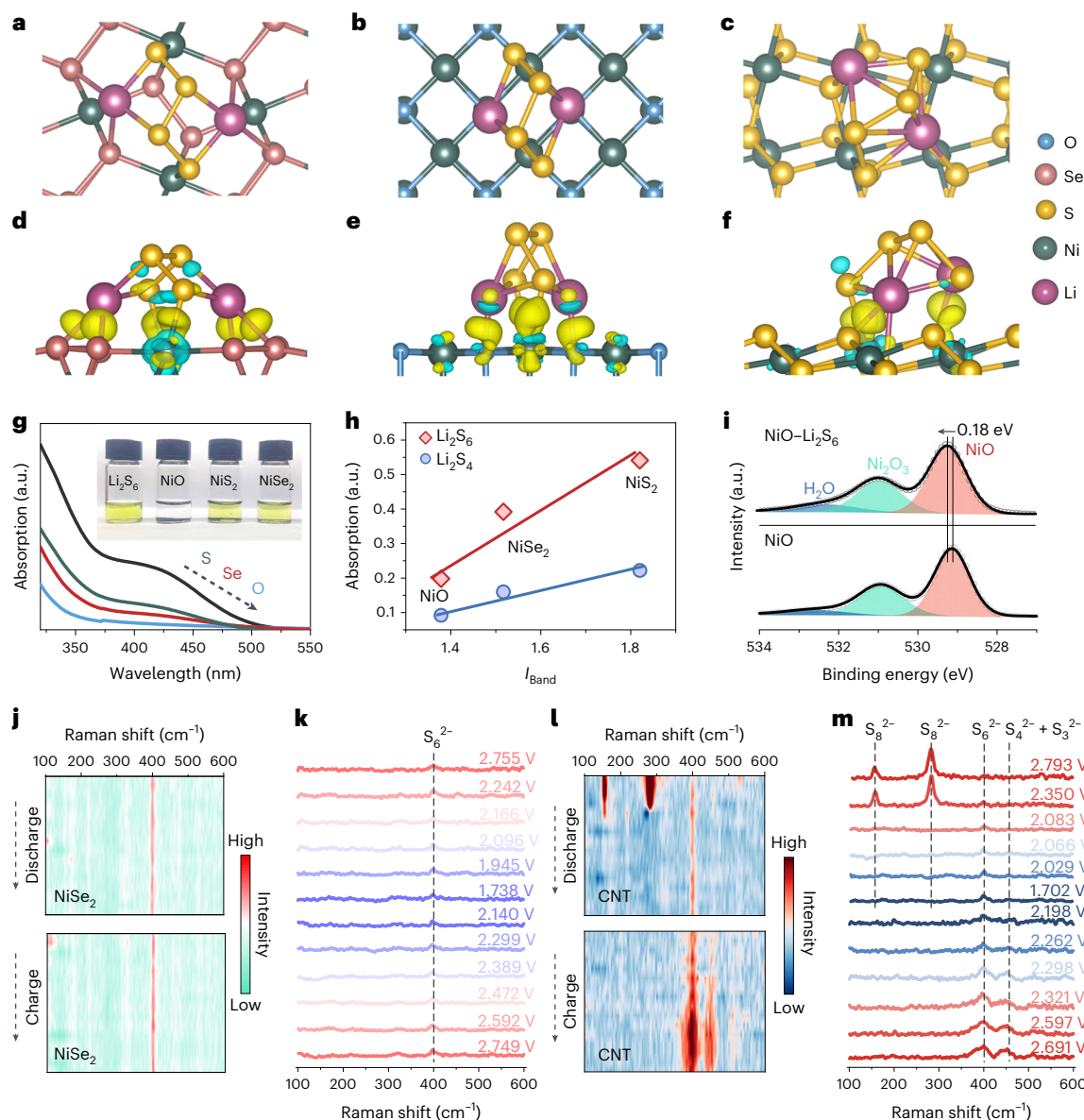
Fig. 2 | The influence of anions in TMCs from an electronic aspect.
a–**c**, Configuration model of Li_2S_4 on the surface of $NiSe_2$ (**a**), NiO (**b**) and NiS_2 (**c**) catalysts. **d**–**f**, Electron-density difference analysis of Li_2S_4 on the surface of $NiSe_2$ (**d**), NiO (**e**) and NiS_2 (**f**) catalysts. The yellow and blue sections represent charge accumulation and loss, respectively. **g**, UV–vis absorption spectra and visualization tests of the interaction between LiPSs and Ni-based catalysts.

**h**, UV–vis absorption comparison of Li_2S_6 and Li_2S_4 for NiO, NiS_2 and $NiSe_2$. **i**, O 1s XPS of NiO after (top) and before (bottom) the adsorption test. **j**–**m**, In situ Raman spectra of the electrode with (**j**,**k**) and without (**l**,**m**) $NiSe_2$ during charging and discharging at 0.3 C. **j**,**l**, Contour maps consisting of 16 Raman spectra. **k**,**m**, Raman spectra selected from (**j**) and (**l**), respectively.

structures of the TMCs. To evaluate the relationship between I_{Latt} and the delithiation energy barrier, the potentiostatic intermittent titration technique (PITT) was used (Supplementary Fig. 29). During the charging process from 2.24 to 2.32 V, cells with $NiSe_2$ provided the highest current responses, indicating the substantially rapid reaction kinetics. However, the low current in cells with NiO suggests their sluggish activation process, with a high charge-transfer resistance. Integrating the area of the current–time curve provides a representation of the Li_2S dissolution capacity. The largest integrated area, for cells with $NiSe_2$, suggests they have the largest dissolution capacity, corresponding to a potentiostatic charging test. The PITT tests thus verify the critical role of $NiSe_2$ with low I_{Latt} in the delithiation process, by weakening the Li–S bond in Li_2S.

For the lithiation process, we focused on E_a for the rate-determining step from Li_2S_4 to Li_2S_2 using various Ni-based TMCs. A voltage of 2.0 V,

corresponding to the conversion step from Li_2S_4 to Li_2S_2, was chosen to achieve the charge-transfer resistance in a standard carbon nanotube (CNT)/sulfur composite cathode (Fig. 3a,b). The charge-transfer resistance at different temperatures reveals a linear relationship between the inverse of absolute temperature and the logarithm of the reciprocal of the charge-transfer resistance (Fig. 3c). The derived E_a values shows that the cells with $NiSe_2$ have the lowest E_a (0.39 eV), lower than those with NiS_2 (0.43 eV) and NiO (0.46 eV), or a pure CNT (0.50 eV), consistent with the predictions of I_{Latt} and the electrochemical tests (Fig. 3d). Cyclic voltammetry (CV) was next conducted to investigate the sulfur reduction kinetics on the electrode under scanning rates from 0.1 mV s^{-1} to 0.5 mV s^{-1} between 1.7 V and 2.8 V (versus Li/Li$^+$). Figure 3e–g presents the contour plots of the CV patterns for NiO, NiS_2 and $NiSe_2$, respectively. The two cathodic peaks at ~2.28 V (peak A) and ~1.96 V (peak B) correspond to the reduction of S_8 to LiPSs and
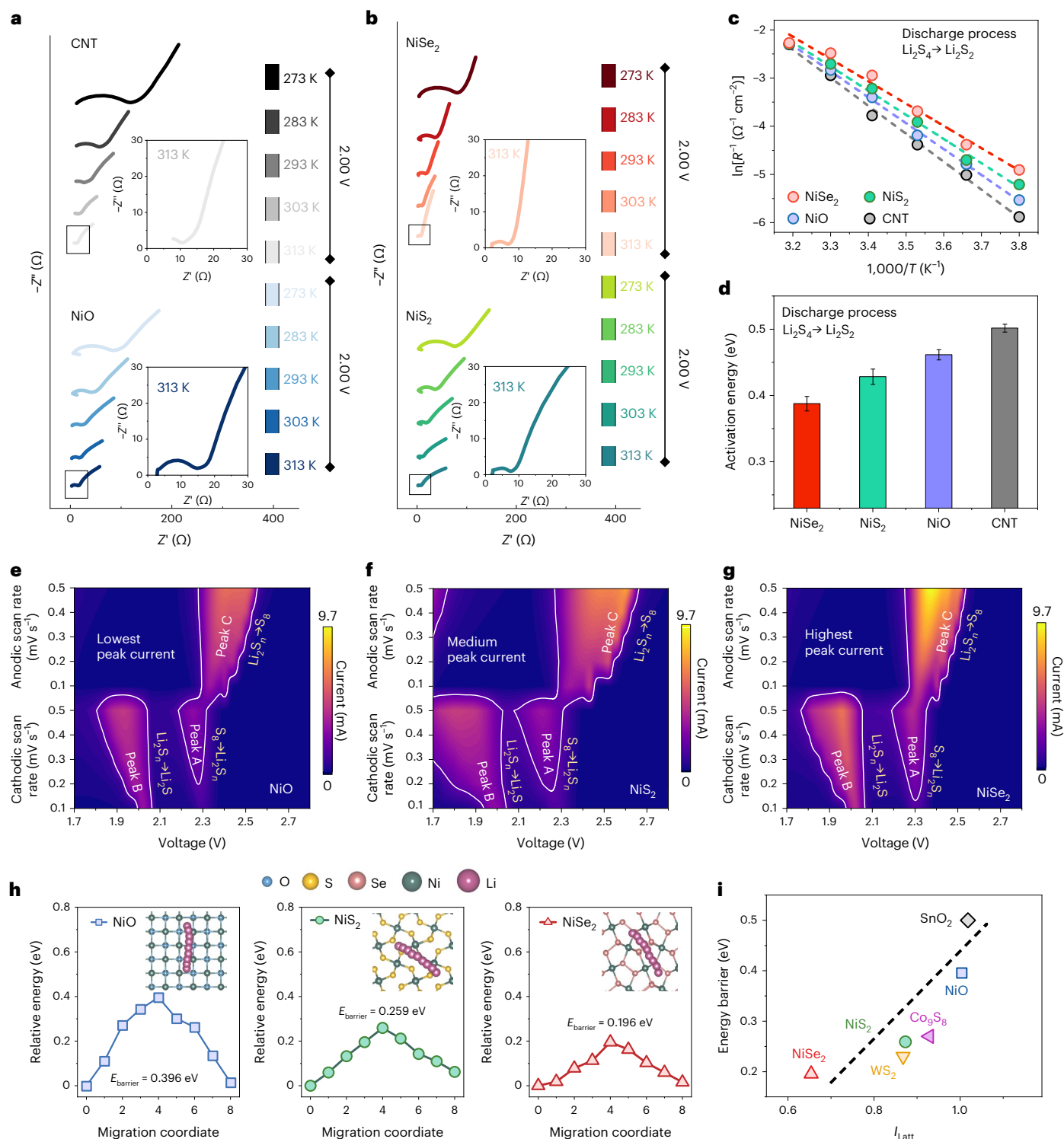
Fig. 3 | The influence of anions in TMCs from a structural aspect. a,b, EIS measurements at various temperatures at 2.0 V of Li–S batteries with different catalysts: CNT and NiO (**a**) and NiSe$_2$ and NiS$_2$ (**b**). Insets: expansions of the boxed regions. **c**, The linear relationship between the inverse of absolute temperature (*T*) and the logarithm of the reciprocal of the charge-transfer resistance. **d**, Activation energies for the step from Li$_2$S$_4$ to Li$_2$S$_2$ of the sulfur redox reactions for the various Ni-based catalysts. The error bars for all catalysts were determined from the standard deviation. **e–g**, Contour plots of CV patterns for NiO (**e**), NiS$_2$ (**f**) and NiSe$_2$ (**g**) with different scan rates. **h**, Energy profiles for the diffusion process of Li$^+$ on NiO, NiS$_2$ and NiSe$_2$. Insets: top-view schematic representations of the corresponding diffusion pathways for NiO, NiS$_2$ and NiSe$_2$. **i**, The relationship between diffusion energy barrier (*E*$_{barrier}$) and *I*$_{Latt}$.

Li$_2$S$_2$/Li$_2$S. The anodic peak at ~2.37 V (peak C) in the anodic sweep results from the transition from Li$_2$S$_2$/Li$_2$S to LiPSs and S$_8$. The cathode with NiSe$_2$ shows a higher current response than those with NiO and NiS$_2$, especially in the region where Li$_2$S$_2$/Li$_2$S transitions to LiPSs and S$_8$,

corresponding to the PITT results. Meanwhile, with the decrease in scan rates, the cathode with NiSe$_2$ still exhibits an obvious current response. Those peaks (peaks A and C) for all three TMC-containing electrodes have a linear relationship with the square root of the scanning rates

(Supplementary Fig. 30), indicating a diffusion-limited process. The following classical Randles–Sevcik equation was applied to describe the lithium diffusion process:

$$I_P = \left(2.69 \times 10^5\right) n^{1.5} S D_{Li+}^{0.5} C_{Li+} v^{0.5} \tag{1}$$

where I_P is the peak current, n is the charge-transfer number, S is the geometric area of the active electrode, D_{Li+} is the Li-ion diffusion coefficient, C_{Li+} is the concentration of Li$^+$ in the cathode and v is the potential scan rate. The slope of the curve ($I_P/v^{0.5}$) represents the Li-ion diffusion rate, as n, S and C_{Li+} are unchanged. It can be seen that the cell with NiO exhibits the lowest Li-ion diffusivity, which mainly arises from the high I_{Latt} and strong LiPS adsorption, leading to catalyst passivation, the shuttle effect and increased electrolyte viscosity. In contrast, the electrode with NiSe$_2$, with its low I_{Latt}, demonstrates much faster diffusion because of the decreased electrolyte viscosity.

A galvanostatic intermittent titration technique (GITT) was used (Supplementary Fig. 31) to calculate the chemical diffusion coefficient using the equation derived from Fick's second law:

$$D_{Li^+} = \frac{4}{\pi\tau}\left(\frac{n_m V_m}{S}\right)^2 \left(\frac{\Delta E_S}{\Delta E_t}\right)^2 \tag{2}$$

where τ is the duration of the current pulse, n_m is the mole number of the electrode materials, V_m is the molar volume of the electrode materials, S is the contact area between electrode and electrolyte, ΔE_S is the change in the steady-state voltage at the end of the relaxation period over a single galvanostatic titration and ΔE_t is the total change of cell voltage during a constant-current pulse. The cell with NiSe$_2$ has the highest Li$^+$ diffusion coefficient (7.84×10^{-12} cm^2 S^{-1}) when compared with those with NiO (2.91×10^{-12} cm^2 S^{-1}) and NiS$_2$ (7.35×10^{-12} cm^2 S^{-1}), indicating a decreased electrolyte viscosity. The lower electrolyte viscosity of cells with NiSe$_2$ directly corresponds to the reduced shuttle effect, which can be attributed to the faster charge-transfer kinetics or superb sulfur-reduction kinetics.

We also calculated the diffusion barriers for Li$^+$ on Ni-based TMCs (Fig. 3h). The diffusion pathways on the TMC surfaces follow the arc curves from one stable point to another, with the saddle point located in the middle of the pathway. The diffusion barrier for Li$^+$ along the diffusion coordinate on NiSe$_2$ is 0.196 eV, less than for NiS$_2$ (0.259 eV) and NiO (0.396 eV). We also summarize the recent catalytic materials and assess the relationship between the I_{Latt} of the TMCs and the relative energy barrier for the diffusion processes of Li$^+$ (Fig. 3i). As I_{Latt} increases from 0.65 (NiSe$_2$) to 1.02 (SnO$_2$), the diffusion energy barrier climbs from 0.196 eV to 0.5 eV. The scaling relationship confirms that I_{Latt} plays a vital role in Li$^+$ diffusion, suitable for different TMCs. A lower barrier for Li$^+$ diffusion is believed to increase the diffusion rate on the surface of the TMCs, promoting the reaction between the lithium and sulfur.

### Development of BD scaling with catalytic activity

As discussed already, the electronic and structural descriptors, I_{Band} and I_{Latt}, are correlated to adsorption and reaction processes, respectively. A low I_{Band} suggests a high adsorption ability of the TMCs, but may cause the passivation of catalysts with too low a value. The low I_{Latt} stretches the Li–S bond in adsorptive lithium (poly)sulfides, decreasing the energy barrier for the reaction. For a typical catalytic reaction in a Li–S battery, there is a cycle of LiPS adsorption, reaction and desorption occurring at the surface of the catalyst[12]. It is thus believed that the catalytic activity can be understood more comprehensively by simultaneously considering I_{Band} and I_{Latt}, as shown in Fig. 4a. For TMCs with low I_{Band} and high I_{Latt}, like NiO, the strong interaction and high energy barrier for lithiation and delithiation passivates the surface of the catalyst and lowers the catalytic activity. Those TMCs with high I_{Band} and moderate I_{Latt}, like NiS$_2$, have moderate catalytic activity, but the weak interaction makes LiPSs diffuse towards the anodes, leading to the

shuttle effect. Only with TMCs with moderate I_{Band} and low I_{Latt}, like NiSe$_2$, does medium adsorption accelerate the LiPS conversion promptly.

To verify the predicted electrocatalytic properties of the different TMC catalysts, the same amount of catalyst was loaded onto an electrode and the CV curves of symmetric cells with Li$_2$S$_6$-containing electrolyte were measured (Fig. 4b). Upon polarization, Li$_2$S$_6$ is converted into higher-order and lower-order polysulfides at the anodes and cathodes, respectively. The electrode with NiSe$_2$ shows the largest peak area, highest peak current response and lowest polarization compared with NiS$_2$ and NiO, indicating its high capability to improve LiPS redox kinetics. The current response with Li$_2$S$_6$ presented in the chronoamperometry curves is much higher than that for the cells without Li$_2$S$_6$ (Supplementary Fig. 32), implying that the lithiation/delithiation reaction is responsible for the current response rather than the double-layer capacitance. The highest current response of the electrode with NiSe$_2$ indicates strong catalytic LiPS conversion. Furthermore, the EIS of the NiSe$_2$-contained symmetric cell also exhibits the lowest charge-transfer impedance (Fig. 4c), indicating the lowest charge-transfer barrier at the NiSe$_2$/LiPS interface, which also contributes to the fast conversion of LiPSs.

To further ascertain the distinct catalytic performances of the samples towards oxidation and reduction reactions in Li–S batteries, CV analyses were performed on asymmetric cells employing Ni-based TMCs/S as the cathode and Li foil as the anode (Supplementary Fig. 33a). The resulting CV curves distinctly reveal two sets of reversible redox peaks. Notably, in cells with S@CNT/NiSe$_2$, two cathodic peaks (A and B), corresponding to the conversion of S$_8$ to Li$_2$S$_n$ ($6 \leq n \leq 8$) and Li$_2$S$_n$ ($2 \leq n \leq 4$) to Li$_2$S, exhibit both higher voltages and intensities, while the two anodic peaks (C and D), corresponding to the transformation from Li$_2$S to Li$_2$S$_n$ and eventually to S$_8$, appear at lower potentials compared to those with NiO or NiS$_2$. These peak shifts indicate a diminished energy barrier for Li–S redox reactions, attributed to the interaction between NiSe$_2$ and LiPSs as well as Li$_2$S. Enhanced current densities of peaks within NiSe$_2$-incorporated electrodes further underscore accelerated reaction kinetics for the liquid–solid conversion, probably leading to reduced soluble LiPSs in the electrolyte, thereby mitigating the shuttle effect. To probe the catalytic effect during electrochemical processes, Tafel plots were constructed based on peaks A and D from the CV profiles. For the reduction process, the fitted slopes for cathodes with NiO, NiS$_2$ and NiSe$_2$ are 70.56, 65.60 and 58.18 mV dec^{-1}, respectively (Supplementary Fig. 33b). For the oxidation process, the corresponding slopes are 162.09, 129.42 and 60.23 mV dec^{-1}, respectively (Supplementary Fig. 33c). Reduced slopes during both reduction and oxidation for the NiSe$_2$-containing cathode suggest its favourable catalytic activity in the redox conversion between LiPSs and Li$_2$S.

Potentiostatic nucleation experiments were next conducted to unveil the nuanced role of anions within TMCs on the distribution of solid Li$_2$S subsequent to the decomposition of LiPSs. According to Faraday's law, the specific capacities for Li$_2$S precipitation on the NiO, NiS$_2$ and NiSe$_2$ cathode were calculated as 188.4, 196.0 and 217.5 mAh g^{-1}, respectively (Supplementary Fig. 34). Evidenced by the elevated Li$_2$S precipitation capacity on NiSe$_2$-incorporating cathodes, superior reaction kinetics from LiPSs to Li$_2$S were deduced, ascribed to moderate adsorption and facile dissociation. Post-Li$_2$S precipitation, the cathode surfaces were scrutinized (Supplementary Fig. 35). NiO-loaded samples displayed non-uniform dispersion of small Li$_2$S particles due to localized catalyst passivation. NiS$_2$ surfaces featured larger yet isolated Li$_2$S islands. In contrast, NiSe$_2$ surfaces exhibited thicker, more uneven Li$_2$S deposition, aligning with a higher deposition capacity. Employing the same solvent, the distinct deposition morphology was attributed to the embedded highly active NiSe$_2$. To decipher the diverse Li$_2$S growth behaviours, dimensionless diagnostic analysis of current–time curves from Li$_2$S nucleation tests was performed using Scharifker–Hills models (Fig. 4d). 3DI and 3DP indicate the instantaneous (I) or progressive (P) nucleation of a three-dimensional (3D) hemispherical nucleus
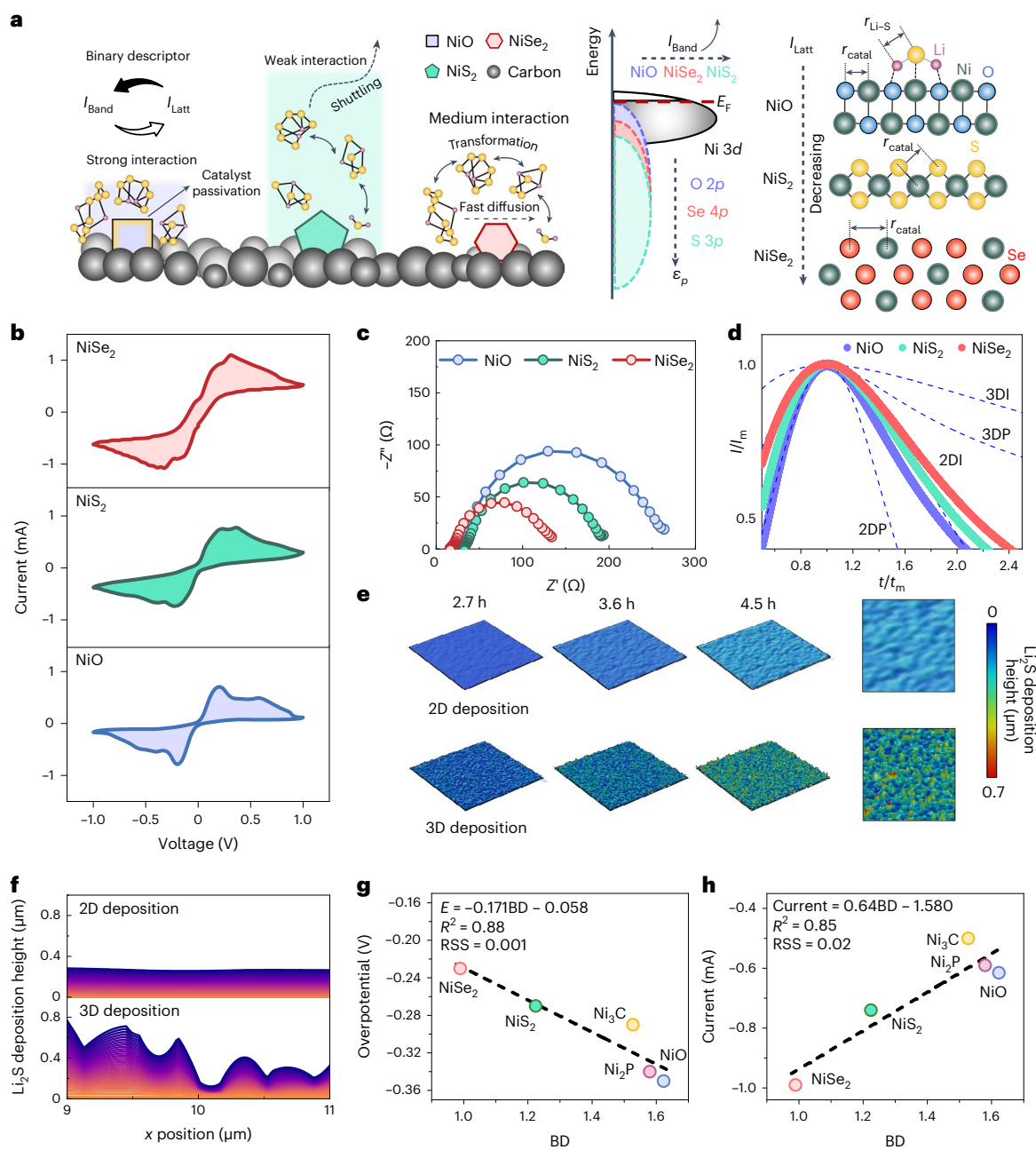
Fig. 4 | Development of a BD to reveal the influence of anions on catalytic processes. a, Schematic of the influence of anions (O, S and Se) on the catalytic process, simultaneously considering electronic and structural effects. **b**, CV curves of symmetric cells using Ni-based catalysts at a scan rate of 0.1 mV s⁻¹. **c**, EIS of Li₂S₆ symmetric cells. **d**, Dimensionless current–time transients of NiO, NiS₂ and NiSe₂ to perform peak fitting according to theoretical 2D and 3D models. I_m (peak current) and t_m (time needed to achieve the peak current)

can be detected from the current–time transients. *I* is the tested current from Li₂S nucleation experiments. **e**, COMSOL simulations for the Li₂S deposition morphology evolution upon discharging at the cathodes with low and high reaction kinetics. **f**, The Li₂S height map across the different positions of the cathode with low and high reaction kinetics. **g,h**, Linear regression fitting between the overpotential (**g**) and peak current (**h**) and the BD.

with a growth rate controlled by ion diffusion. 2DI and 2DP suggest a two-dimensional (2D) nucleation mechanism with a growth rate controlled by lattice incorporation. Transitioning from NiO to NiS₂ and NiSe₂, the Li₂S growth mode evolved from a 2DI model to a 3DP model, indicating the efficacy of NiSe₂ in prompting instantaneous nucleation and dense Li₂S growth. COMSOL simulations were used to illuminate the influence of catalytic activity on Li₂S deposition morphology (for more information, see Supplementary Note 3). At the beginning of the deposition process, the cathode surface with low reaction kinetics is clean, with barely any observed Li₂S nuclei due to the high reaction-

energy barrier (Fig. 4e). Subsequently, as the discharge process progresses, Li₂S nuclei form on the cathode surface until under a high overpotential, and the lateral growth is inhibited once they come into contact. The long time required for Li₂S nucleation limits the disproportionation reactions, producing a 2D-like deposition morphology. In contrast, the introduction of catalysts with high catalytic activity, such as NiSe₂, results in a cathode surface with numerous nucleation sites. The early-formed Li₂S sites act as anchors for disproportionation reactions, promoting the 3D deposition of Li₂S. The greater height difference across the surface of the cathodes with
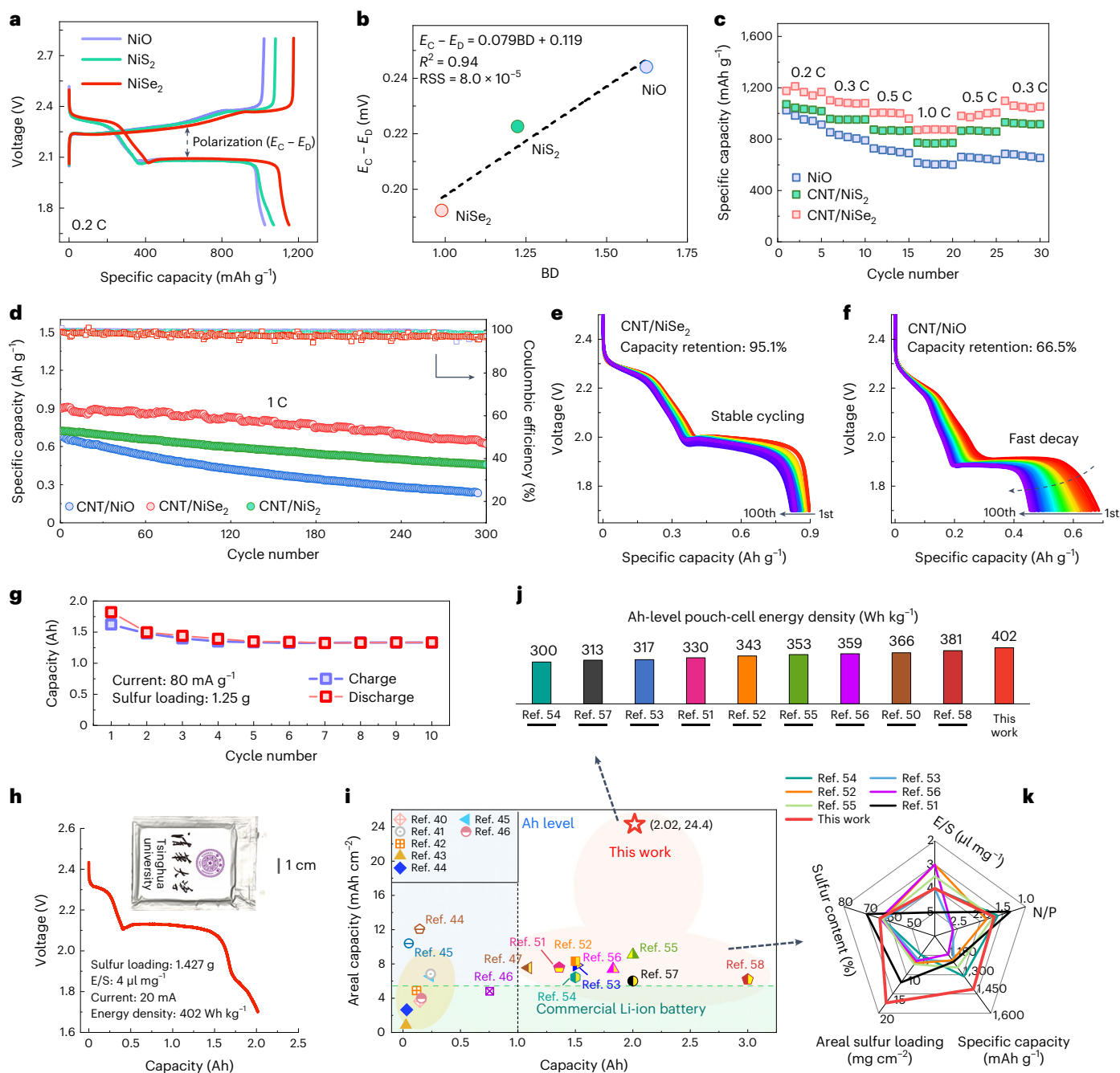
Fig. 5 | The influence of anions in TMCs on the electrochemical performance of cathodes. a, Discharge and charge profiles of S@CNT/NiO, S@CNT/NiS$_2$ and S@CNT/NiSe$_2$ with a sulfur loading of ~2 mg cm^{-2}. E_C, charge voltage; E_D, discharge voltage. **b**, Linear regression fitting between the overpotential and the BD. **c**, Rate performance of different cathodes. **d**, Long-term cycling stability of different cathodes at 1 C for 300 cycles. **e,f**, Corresponding charge–discharge profiles of CNT/NiSe$_2$-based (**e**) and CNT/NiO-based (**f**) cells during the first 100 cycles. **g**, Cycling performance of a 1.25 g sulfur pouch cell using NiSe$_2$ catalyst. **h**, Photograph and discharge profile of a 1.427-g-sulfur pouch cell, which delivers a high gravimetric energy density of 402 Wh kg^{-1}. **i–k**, Performance comparison of this work and previously reported Ah-level Li–S batteries. **i**, Capacity versus areal capacity comparison between this work and previously reported results. **j**, The state-of-the-art performance of high-energy-density (over 300 Wh kg^{-1}) Li–S pouch cells from published literature and this work. **k**, Performance comparison between this work and previously reported Li–S pouch cells. N/P, negative/positive ratio signifying ratio between anode and cathode capacity.

high reaction kinetics than those with low kinetics confirms the deposition morphology difference (Fig. 4f), consistent with the higher deposition capacity of cathodes containing NiSe$_2$. The oxidation of deposited Li$_2$S was also investigated using a potentiostatic charging process (Supplementary Fig. 36). NiSe$_2$ exhibited much higher dissolution capacity than NiO and NiS$_2$, indicating the more effective oxidation process on NiSe$_2$ surfaces. To further quantify the analysis model in Fig. 4a for the catalytic effect in Li–S batteries, we developed a BD

$\left(\lambda_1 \left| \frac{\varepsilon_s - \varepsilon_p}{\varepsilon_s} \right| + \lambda_2 \left| \frac{\varepsilon_p - \varepsilon_d}{\varepsilon_p} \right| + \lambda_3 \frac{r_{\text{Li-S}}}{r_{\text{catal}}} \right)$ considering the influence of both orbital coupling and structural distortions on catalytic activity. The linear combination with I_{Band} and I_{Latt} as mutually independent features was chosen here to provide a more in-depth understanding of the catalysis dynamics and avoid the overfitting issue. The coefficients (λ_1, λ_2, λ_3) for linear combination symbolize the relative importance of either the electronic effect (s–p and d–p hybridization) or the structural effect (for further details, see Supplementary Table 8).

As a comprehensive descriptor, BD assesses the catalytic activity encompassing not only surface reactions but also adsorption and diffusion. As widely used important indicators for evaluating catalyst activity, the overpotential and peak current in the CV also indicate the combined effects of adsorption, reaction and diffusion processes. Therefore, we used overpotential and peak current to search for the coefficient combinations of BD, aiming to correlate microscopic mechanisms (orbital coupling and crystal structure distortions) and macroscopic catalytic activity. Ni_2P and Ni_3C were additionally synthesized and tested to improve the validity of the BD (Supplementary Figs. 37 and 38). The overpotential and peak currents of all five samples (NiO, NiS_2, $NiSe_2$, Ni_2P and Ni_3C) were used to determine the coefficients of each item in the BD. Note that the satisfying indicator cannot be artificially proposed due to the complex fitting limits. Trial-and-error methods are inappropriate because of the excessive possible coefficient combinations. From the data science perspective, this is a typical multi-objective optimization problem, specifically a bicriteria optimization, which the machine-learning approach can effectively solve. Therefore, a machine-learning analysis using Monte Carlo simulation and the genetic algorithm was conducted to optimize the coefficient combinations (Supplementary Note 4). Specifically, the genetic algorithm was used to efficiently search for possible combinations, and the Monte Carlo simulation guaranteed statistical confidence during generation of the search space. Moreover, the Monte Carlo simulation can also handle the uncertainties in the model performance due to random initializations when applying the genetic algorithm. A potential solution was thus obtained as follows:

$$BD = -0.16039 \frac{\varepsilon_s - \varepsilon_p}{\varepsilon_s} + 0.24661 \frac{\varepsilon_p - \varepsilon_d}{\varepsilon_p} + 1.54370 \frac{r_{\text{Li–S}}}{r_{\text{catal}}} \quad (3)$$

Simultaneously satisfying the fitting results (Fig. 4g,h) for overpotential ($R^2 = 0.88$) and peak current ($R^2 = 0.85$) was achieved, considerably surpassing the $\frac{\varepsilon_s - \varepsilon_p}{\varepsilon_s}$-only ($R^2 = 0.21$ for the overpotential and $R^2 = 0.44$ for the peak current) or $\frac{\varepsilon_p - \varepsilon_d}{\varepsilon_p}$-only ($R^2 = 0.34$ for the overpotential and $R^2 = 0.46$ for the peak current) descriptor (Supplementary Figs. 39 and 40). Although the fitting result of I_{Latt} to overpotential ($R^2 = 0.88$) is the same as for the BD ($R^2 = 0.88$), the much lower fitting accuracy to peak current of I_{Latt} ($R^2 = 0.51$) than BD ($R^2 = 0.85$) indicates that I_{Latt} cannot optimize the two objective functions simultaneously (Supplementary Fig. 41). The higher coefficient for I_{Latt} highlights its importance for the catalytic activity due to its relevance to the reaction energy barrier and diffusion resistance. A series of non-Ni-based TMCs were further tested, validating the applicability of the BD and indicating its superior capability in guiding catalyst design for Li–S batteries (Supplementary Table 9 and Supplementary Figs. 42 and 43).

Electrochemical properties of Li–S batteries

The electrochemical performance of the Li–S batteries was investigated to verify the influence of the anions of TMCs on Li–S redox reactions. Figure 5 shows the electrochemical properties of Li–S batteries using the designed catalysts. Figure 5a shows the galvanostatic discharge–charge profiles with an areal-sulfur mass loading of 2.0 mg cm^{-2} at 0.2 C. The cells containing $NiSe_2$ delivered a higher capacity (1,150 mAh g^{-1}) than those with NiS_2 and NiO (1,071 and 1,024 mAh g^{-1}, respectively). These results suggest that $NiSe_2$ has higher catalytic activity, consistent with the lower polarization overpotentials of $NiSe_2$ (0.16 V) compared to NiS_2 (0.22 V) and NiO (0.24 V). Notably, the predicted overpotentials based on BD showed a good correspondence with the experimental values, with high fidelity ($R^2 = 0.94$, residual sum of squares (RSS) = 8.0×10^{-5}; Fig. 5b). The polarization decreased with decreasing BD, suggesting that the $NiSe_2$, with the lowest BD, is more catalytically effective. The rate abilities of S@CNT and various S@CNT/TMCs were also measured to compare their reaction kinetics for Li–S chemistry

with a sulfur loading of ~2 mg cm^{-2} (Fig. 5c). The capacity at different rates increased as BD decreased from NiO to NiS_2 and $NiSe_2$, consistent with theoretical predictions. The surface of NiO, with high BD, is easily passivated due to the strong interaction with LiPSs and the high reaction energy barrier for the rate-determining step. The NiS_2, with a middle value of BD, is catalytically active but weakly interacts with LiPSs, resulting in the shuttle effect. The $NiSe_2$, with low BD, shows the best effect due to medium adsorption and a low reaction energy barrier. Long-term cycling stability with high capacity retention is crucial for the practical application of Li–S batteries, so we compared the long-cycling stability of different samples at 1 C. After 300 cycles, the S@CNT/NiSe$_2$ cathode maintained a discharge capacity of 624.7 mAh g^{-1}, giving an average capacity decay rate of 0.101% per cycle (Fig. 5d). The S@CNT/NiSe$_2$ cathode achieved a high capacity retention of 95.1% during the first 100 cycles (Fig. 5e). By contrast, the S@CNT/NiO cathode severely decayed to 66.5% during the first 100 cycles due to surface passivation by LiPSs (Fig. 5f). Those with NiS_2 decayed gradually to 85% because of the weak interaction with LiPSs (Supplementary Fig. 44). The improvements in cycling stability are ascribed to the moderate binding of $NiSe_2$ with soluble LiPSs and the fast desorption of precipitates.

To demonstrate the capability of the S@CNT/NiSe$_2$ in practical applications, high-energy-density Li–S batteries under high sulfur loading were examined. Two distinct voltage plateau profiles were still present even with 8.2 mg cm^{-2} (Supplementary Fig. 45), suggesting the accelerated reaction kinetics achieved with $NiSe_2$. Moreover, stable cycling was attained with high initial areal capacities of 3.70, 5.16 and 8.24 mAh cm^{-2} for sulfur loadings of 3.6, 5.7 and 8.2 mg cm^{-2}, respectively (Supplementary Fig. 46). With a sulfur loading of 15.0 mg cm^{-2} and an electrolyte/sulfur ratio of 8.0 μl mg^{-1}, the S@CNT/NiSe$_2$ cell still had an initial areal capacity of 18.50 mAh cm^{-2} in the first cycle (Supplementary Fig. 47), better than state-of-the-art LiNi$_x$Co$_y$Mn$_{1-x-y}$O$_2$-based cathodes (~4 mAh cm^{-2}) and many reported S cathodes[11,34–39]. The performance of the Li–S cells over a wide temperature range from −20 °C to 55 °C was also tested (Supplementary Fig. 48). At high temperature (55 °C), the capacity of samples with and without $NiSe_2$ is similar due to the fast reaction kinetics. However, when the temperature drops below 0 °C, batteries without catalysts cannot charge and discharge normally and show much lower capacity than those with $NiSe_2$ because of the slow reaction kinetics at low temperatures. In contrast, the cell with the CNT/NiSe$_2$ cathode can still clearly present two discharge platforms, higher capacity and low polarization at low temperatures (Supplementary Fig. 49), reflecting its good redox kinetics at low temperatures. Moreover, most of the original capacity is recovered when the temperature increases from −20 °C to 25 °C. Therefore, as predicted by the BD, $NiSe_2$, with its moderate I_{Band} and lowest I_{Latt}, has much higher catalytic ability, ensuring high sulfur utilization and reversible capacities even under ultrahigh sulfur-loading or low temperature, which is promising for use in practical Li–S batteries.

Furthermore, an Ah-level pouch cell with 1.25 g sulfur loading was assembled and tested under a current density of 80 mA g^{-1}. The pouch cell has an initial capacity of 1.82 Ah and shows stable cycling performance (Fig. 5g). We then increased the sulfur loading to 1.427 g and assembled a pouch cell with a high areal-sulfur loading (17.3 mg cm^{-2}) and low E/S (4 μl mg^{-1}). As shown in Fig. 5h, the pouch cell delivers a high specific energy of 402 Wh kg^{-1} based on the whole cell (details are presented in Supplementary Table 10 and Supplementary Fig. 50), suggesting the effectiveness of $NiSe_2$ in improving sulfur utilization under practical conditions. In terms of areal capacity and total capacity, our Li–S pouch cell with $NiSe_2$ catalyst represents a substantial advance and thus achieves higher gravimetric energy density compared with previously reported Li–S batteries (Fig. 5i,j)[40–55]. The intercrossed electron/ion-transport channels of the lightweight 3D foam host (Fig. 5k) ensure a high sulfur content (64.2%) throughout the cathode, comparable to previously reported high-energy-density Li–S batteries. Benefitting

from the favourable catalytic effect of $NiSe_2$, an ultrahigh areal capacity of 24.4 mAh cm^{-2} can be achieved under a relatively low E/S (4 µl mg^{-1}), outperforming most previously reported Ah-level Li–S pouch cells. Note that the specific energy and cycling performance of our Li–S pouch cell could be further enhanced after optimizing the parameters for a mass production process[56,57] or designing cathode tortuosity/porosity[58,59]. Li-metal protection[60–64] and electrolyte design[65–68] are also needed to further improve cell performance.

Conclusions

In summary, we have applied DFT to identify an experimentally validated BD simultaneously considering the electronic and structural properties of the catalytic systems to guide the design of highly efficient catalysts for Li–S batteries. A genetic algorithm is used to search coefficient combinations in large parameter spaces, with Monte Carlo simulations validating the uncertainties. I_{Band} and I_{Latt} are developed to describe the electronic and structural effects of TMCs, respectively. Specifically, a low I_{Band} enhances the adsorption but may passivate the catalysts when the value is too low. Low I_{Latt} stretches and weakens the Li–S bond of adsorptive lithium (poly)sulfides, thus accelerating delithiation and lithiation on the TMC surfaces. To prove its effectiveness, the BD was used to decipher the role of anions in regulating LiPS conversion kinetics, using Ni-based TMCs (NiO, NiS_2, $NiSe_2$, Ni_2P and Ni_3C) as a model system. $NiSe_2$ with a low BD is predicted to have higher catalytic activity, in good agreement with experiments. The Li–S battery with $NiSe_2$ shows the lowest electrochemical barrier for LiPSs reduction/Li_2S oxidation and the best battery performance among the Ni-based TMCs, even with a high sulfur loading of 15.0 mg cm^{-2} or under low temperatures. An Ah-level Li–S pouch cell delivering a practical specific energy of 402 Wh kg^{-1} also demonstrates its potential in high areal-sulfur loading (17.3 mg cm^{-2}) and lean-electrolyte (E/S of 4 µl mg^{-1}) operations. The proposed BD, composed of electronic and structural aspects, offers a rational viewpoint from which to analyse LiPS conversion and to design efficient catalysts and could be further applied to other TMCs as a universal descriptor.

Methods

Characterization of materials

XRD was conducted by using a Bruker D8 Advance diffractometer using Cu Kα emission (λ = 1.5406 Å). Scanning electron microscopy and energy-dispersive X-ray spectrometer measurements were conducted on a field-emission scanning electron microscope (SU 8010) at 5 kV. High-resolution transmission electron microscopy (FEI Titan G2 80-200) was used to investigate microstructure and morphology. Elemental maps and high-angle annular dark-field scanning transmission electron microscopy images were obtained at 200 kV. Inductively coupled plasma atomic emission spectroscopy (TJA RADIAL IRIS 1000) was used to determine the mass content. XPS spectra were measured on an ESCALAB 250Xi system to investigate the components of the catalysts. In situ Raman (Lab RAM HR Evolution) tests were performed to demonstrate the alleviation of the shuttle effect.

Li_2S_6 symmetric cells measurements

Symmetric cells were assembled with TMCs/CNTs or CNTs as the electrode and 40 µl of 0.5 M Li_2S_6 solution as the electrolyte. Another 10 µl of the electrolyte was dropped on the separator. The CV profiles of symmetric cells were tested at a scan rate of 1 mV s^{-1} between −1.0 and 1.0 V.

Li_2S_6 adsorption test

A 5 mM Li_2S_6 solution was prepared by mixing sulfur and lithium disulfide (5:1, molar ratio) in dimethoxyethane (DME) under vigorous stirring. Then, catalyst powder was added to the Li_2S_6/DME solution for visual comparison. The same surface area was controlled by adjusting the amount of catalyst powder based on the specific surface area (Supplementary Fig. 20).

Li_2S nucleation test

Sulfur and lithium disulfide were mixed in a molar ratio of 7:1 in tetraglyme under vigorous stirring to prepare the 0.5 M Li_2S_8. A 20-µl volume of the Li_2S_8 electrolyte was dropped onto the cathode side (TMCs/CNTs or CNTs), and 20 µl of the conventional electrolyte was dropped onto the lithium anode side. After galvanostatically discharging to 2.06 V at a current of 0.134 mA, the cells were potentiostatically discharged at 2.05 V until the current was lower than 0.001 mA. The nucleation capacity was calculated by the integrated area of the plotted curve using Faraday's law.

Li_2S dissolution test

After Li_2S deposition, the cells were disassembled, and the cathodes were washed with DME to remove the unreacted LiPSs. The cathodes were then used to assemble new cells with lithium anodes and conventional electrolytes for Li_2S dissolution. The cells were potentiostatically charged at 2.35 V until the charge current was below 0.001 mA to achieve the complete dissolution of Li_2S.

Electrochemical measurements of batteries

Sulfur was impregnated into CNTs using a melt-diffusion method at 155 °C for 10 h according to previous reports, resulting in S/CNT composites with a 70 wt% or 80 wt% sulfur content. The cathode was prepared by mixing S-CNT powder (70 wt% sulfur content), conductive carbon (CNT), polyvinylidene fluoride and TMCs (NiO, NiS_2 and $NiSe_2$) with a mass ratio of 7:1:1:1 in N-methylpyrrolidone to form a slurry, which was then cast onto Al foil and vacuum-dried at 60 °C. Lithium metal foil was used as the anode. The conventional electrolyte was composed of 1,3-dioxolane (DOL) and DME (1:1 by volume) solution containing 1 M dilithium (trifluoromethane sulfonylimide) imide (LiTFSI) and 1 wt% LiNO$_3$. A 40-µl volume of electrolyte was added to the cell. The cells were assembled in a glove box filled with argon. A LAND 2001A battery testing system was used to test the galvanostatic charge–discharge performance, and the potential range was set from 1.7 V to 2.8 V (versus Li/Li$^+$). A VMP3 electrochemical workstation (Bio Logic) was used for the CV and EIS tests. The frequency range of the EIS test was between 10 MHz and 0.1 Hz with a 5-mV amplitude. For the shuttle-current measurements, the batteries were charged and discharged over three cycles before being galvanostatically charged to 2.8 V with a current density of 0.2 C. The batteries were then discharged to 2.38 V and switched to a potentiostatic mode, where the shuttle current reached a maximum. After 3×10^4 s, the potentiostatic current was stabilized and recorded as the shuttle current. For the GITT test, a constant current density of 0.2 A g^{-1} was adopted for 1 h followed by a pulse of duration of 5 h to collect the potential response. For the PITT test, cells were potentiostatically charged from 2.24 to 2.32 V. The current was recorded to study the delithiation process of Li_2S.

Assembly of Li–S pouch cells

Typically, for the sulfur cathodes used for pouch cells, S/CNT composites (80 wt% sulfur content), conductive carbon (acetylene black), polyvinylpyrrolidone binder and $NiSe_2$ in a mass ratio of 18:0.5:0.5:1 were well ground and subsequently dispersed in 10 ml of ethanol/H$_2$O (1:5 in volume) solution. Afterwards, the solution was magnetically stirred for 12 h. The obtained slurry was dropped onto a rectangular CNT-loaded melamine foam with a thickness of 1.5 mm, which was then transferred to a 60 °C heating plate to promote the evaporation of the ethanol/H$_2$O, resulting in a sulfur cathode for use in pouch-cell assembly. The total sulfur loading and areal-sulfur loading of the as-prepared cathodes could be adjusted by manipulating the amount of S/CNT composites and the area of the rectangular foam electrode. The foam electrode was used as the cathode, and lithium foil (200 µm), ceramic-coated polyethylene separator and Al-plastic film were used as the anode, separator and package material, respectively. The electrolyte was DOL/DME (1:1, by volume) with 0.6 M LiTFSI and 0.4 M LiNO$_3$ additives. An

Al foil was attached to the surface of the foam to facilitate welding of the Al tab. Similarly, a piece of Cu foil was pressed to the lithium foil for welding of the Ni tab.

DFT calculations

Collinear spin-polarized DFT calculations were performed using the Vienna Ab initio Simulation Package (VASP)[69,70] with the generalized gradient approximation Perdew–Burke–Ernzerhof[71] functional. Projected augmented wave potentials[72,73] were chosen to describe the ionic cores, and valence electrons were considered using the plane-wave basis set with a kinetic energy cutoff of 520 eV. Partial occupancies of the Kohn–Sham orbitals were allowed using the Gaussian smearing method with a width of 0.03 eV. The electronic energy was considered self-consistent when the energy change was smaller than 10^{-5} eV per supercell. The geometry optimization was considered convergent when the residual forces were less than 10^{-2} eV Å^{-1}. Strong on-site electron correlation was considered for the electrons in Ni d orbitals employing the rotationally invariant DFT + U formalism[74] with U_{eff} = 6.2 eV(ref. [75]). The CI-NEB methods were used to calculate the Li-ion migration barriers in the structures[29]. Finally, the E_{ads} were calculated as $E_{ads} = E_{ad/sub} - E_{ad} - E_{sub}$, where $E_{ad/sub}$, E_{ad} and E_{sub} are the total energies of the optimized adsorbate/substrate system, the adsorbate in the structure and the clean substrate, respectively. For the modelling description, the surface was simulated using the symmetric periodic slab model with consecutive slabs separated by a 15 Å vacuum layer. Supercells with 72 Ni and 24 C atoms (Ni$_3$C), 48 Ni and 24 P atoms (Ni$_2$P), 36 Ni and 36 O atoms (NiO), 16 Ni and 32 S atoms (NiS$_2$) and 16 Ni and 32 Se atoms (NiSe$_2$) were used. For all calculations, a 2 × 2 × 1 Gamma k-point grid was used for the Brillouin zone sampling. The atomic coordinates of the optimized models are provided in Supplementary Data 1.

Finite-element method simulations

Based on the finite-element method, we established a numerical model of Li–S batteries in the COMSOL Multiphysics 6.0 platform and simulated the morphology evolution of Li$_2$S deposition. The specific reaction kinetics and thermodynamic equations for S$_8$ to Li$_2$S during discharging[76,77] are described in the Supplementary Information, and the process for Li$_2$S deposition behaviour can be described by

$$R_{Li_2S} = K_{Li_2S} \left(C_{Li^+}{}^2 C_{S^{2-}} - K_{sp,Li_2S} \right) \qquad (4)$$

where R_{Li_2S} is the rate of precipitation of Li$_2$S, K_{sp,Li_2S} is the solubility in the electrolyte, K_{Li_2S} is the rate constant, and C_{Li^+} and $C_{S^{2-}}$ are the concentrations of Li$^+$ and S^{2-} in the electrolyte, respectively. We determined the presence or absence of a catalyst by regulating the reaction kinetics parameters of each step of the polysulfide conversion reaction. Specifically, samples with (without) catalyst corresponded to higher (lower) exchange current density in our simulations.

Data availability

Data are available from the corresponding author upon reasonable request. Source data are provided with this paper.

References

1. Wild, M. et al. Lithium–sulfur batteries, a mechanistic review. *Energy Environ. Sci.* **8**, 3477–3494 (2015).
2. Zhou, G., Chen, H. & Cui, Y. Formulating energy density for designing practical lithium–sulfur batteries. *Nat. Energy* **7**, 312–319 (2022).
3. Peng, L. et al. A fundamental look at electrocatalytic sulfur reduction reaction. *Nat. Catal.* **3**, 762–770 (2020).
4. Shi, Z. X., Ding, Y. F., Zhang, Q. & Sun, J. Y. Electrocatalyst modulation toward bidirectional sulfur redox in Li–S batteries: from strategic probing to mechanistic understanding. *Adv. Energy Mater.* **12**, 2201056 (2022).
5. Wang, P. et al. Emerging catalysts to promote kinetics of lithium–sulfur batteries. *Adv. Energy Mater.* **11**, 2002893 (2021).
6. Chen, H. et al. Catalytic materials for lithium–sulfur batteries: mechanisms, design strategies and future perspective. *Mater. Today* **52**, 364–388 (2022).
7. Tao, X. et al. Balancing surface adsorption and diffusion of lithium–polysulfides on non-conductive oxides for lithium–sulfur battery design. *Nat. Commun.* **7**, 11203 (2016).
8. Zhou, G. et al. Catalytic oxidation of Li$_2$S on the surface of metal sulfides for Li–S batteries. *Proc. Natl Acad. Sci. USA* **114**, 840–845 (2017).
9. Zhao, M. et al. Electrochemical phase evolution of metal-based pre-catalysts for high-rate polysulfide conversion. *Angew. Chem. Int. Ed.* **59**, 9011–9017 (2020).
10. Shi, Z. et al. Manipulating electrocatalytic Li$_2$S redox via selective dual-defect engineering for Li–S batteries. *Adv. Mater.* **33**, e2103050 (2021).
11. Shen, Z. H. et al. Cation-doped Zn–S catalysts for polysulfide conversion in lithium–sulfur batteries. *Nat. Catal.* **5**, 555–563 (2022).
12. Han, Z. Y. et al. Catalytic effect in LiS batteries: from band theory to practical application. *Mater. Today* **57**, 84–120 (2022).
13. Zeng, P. et al. Propelling polysulfide redox conversion by d-band modulation for high sulfur loading and low-temperature lithium–sulfur batteries. *J. Mater. Chem. A* **9**, 18526–18536 (2021).
14. Wang, J. Y. et al. 'Soft on rigid' nanohybrid as the self-supporting multifunctional cathode electrocatalyst for high-performance lithium–polysulfide batteries. *Nano Energy* **78**, 105293 (2020).
15. Li, Z. et al. Engineering oxygen vacancies in a polysulfide-blocking layer with enhanced catalytic ability. *Adv. Mater.* **32**, 1907444 (2020).
16. Tian, Y. et al. Low-bandgap Se-deficient antimony selenide as a multifunctional polysulfide barrier toward high-performance lithium–sulfur batteries. *Adv. Mater.* **32**, 1904876 (2020).
17. Jiang, B. et al. Crystal-facet engineering induced active tin-dioxide nanocatalysts for highly stable lithium–sulfur batteries. *Adv. Energy Mater.* **11**, 2102995 (2021).
18. Li, R. et al. Amorphization-induced surface electronic states modulation of cobaltous oxide nanosheets for lithium–sulfur batteries. *Nat. Commun.* **12**, 3102 (2021).
19. Shen, Z. et al. Rational design of a Ni$_3$N$_{0.85}$ electrocatalyst to accelerate polysulfide conversion in lithium–sulfur batteries. *ACS Nano* **14**, 6673–6682 (2020).
20. Han, Z. et al. Engineering d–p orbital hybridization in single-atom metal-embedded three-dimensional electrodes for Li–S batteries. *Adv. Mater.* **33**, e2105947 (2021).
21. Liu, G. et al. Strengthened d–p orbital hybridization through asymmetric coordination engineering of single-atom catalysts for durable lithium–sulfur batteries. *Nano Lett.* **22**, 6366–6374 (2022).
22. Zhou, J. et al. Deciphering the modulation essence of p bands in Co-based compounds on Li–S chemistry. *Joule* **2**, 2681–2693 (2018).
23. Zhang, Z. et al. Tantalum-based electrocatalyst for polysulfide catalysis and retention for high-performance lithium–sulfur batteries. *Matter* **3**, 920–934 (2020).
24. Wang, M. et al. Nitrogen-doped CoSe$_2$ as a bifunctional catalyst for high areal capacity and lean electrolyte of Li–S battery. *ACS Energy Lett.* **5**, 3041–3050 (2020).
25. Liu, F. et al. Dual redox mediators accelerate the electrochemical kinetics of lithium–sulfur batteries. *Nat. Commun.* **11**, 5215 (2020).
26. Calle-Vallejo, F., Loffreda, D., Koper, M. T. M. & Sautet, P. Introducing structural sensitivity into adsorption–energy scaling relations by means of coordination numbers. *Nat. Chem.* **7**, 403–410 (2015).

27. Wang, R. et al. Bidirectional catalysts for liquid–solid redox conversion in lithium–sulfur batteries. *Adv. Mater.* **32**, e2000315 (2020).

28. Xiao, J. et al. Following the transient reactions in lithium–sulfur batteries using an in situ nuclear magnetic resonance technique. *Nano Lett.* **15**, 3309–3316 (2015).

29. Henkelman, G., Uberuaga, B. P. & Jónsson, H. A climbing image nudged elastic band method for finding saddle points and minimum energy paths. *J. Chem. Phys.* **113**, 9901–9904 (2000).

30. Liu, N. et al. Direct electrochemical generation of supercooled sulfur microdroplets well below their melting temperature. *Proc. Natl Acad. Sci. USA* **116**, 765–770 (2019).

31. Yang, A. et al. Electrochemical generation of liquid and solid sulfur on two-dimensional layered materials with distinct areal capacities. *Nat. Nanotechnol.* **15**, 231–237 (2020).

32. Zhou, G. et al. Supercooled liquid sulfur maintained in three-dimensional current collector for high-performance Li–S batteries. *Sci. Adv.* **6**, eaay5098 (2020).

33. Zhou, G. et al. Electrotunable liquid sulfur microdroplets. *Nat. Commun.* **11**, 606 (2020).

34. Yao, W. et al. P-doped $NiTe_2$ with Te vacancies in lithium–sulfur batteries prevents shuttling and promotes polysulfide conversion. *Adv. Mater.* **34**, e2106370 (2022).

35. Wang, L. et al. Design rules of a sulfur redox electrocatalyst for lithium–sulfur batteries. *Adv. Mater.* **34**, e2110279 (2022).

36. Hou, W. et al. Catalytic mechanism of oxygen vacancies in perovskite oxides for lithium–sulfur batteries. *Adv. Mater.* **34**, e2202222 (2022).

37. Zhao, M., Chen, X., Li, X. Y., Li, B. Q. & Huang, J. Q. An organodiselenide comediator to facilitate sulfur redox kinetics in lithium–sulfur batteries. *Adv. Mater.* **33**, e2007298 (2021).

38. Zhao, C. X. et al. Semi-immobilized molecular electrocatalysts for high-performance lithium–sulfur batteries. *J. Am. Chem. Soc.* **143**, 19865–19872 (2021).

39. Zhao, C. et al. A high-energy and long-cycling lithium–sulfur pouch cell via a macroporous catalytic cathode with double-end binding sites. *Nat. Nanotechnol.* **16**, 166–173 (2021).

40. Luo, L., Li, J., Yaghoobnejad Asl, H. & Manthiram, A. In situ assembled VS4 as a polysulfide mediator for high-loading lithium–sulfur batteries. *ACS Energy Lett.* **5**, 1177–1185 (2020).

41. Zhong, M. E. et al. A cost- and energy density-competitive lithium–sulfur battery. *Energy Stor. Mater.* **41**, 588–598 (2021).

42. Ma, Z. et al. Wide-temperature-range Li–S batteries enabled by thiodimolybdate $[Mo_2S_{12}]^{2-}$ as a dual-function molecular catalyst for polysulfide redox and lithium intercalation. *ACS Nano* **16**, 14569–14581 (2022).

43. Chen, Y. et al. Co–Fe mixed metal phosphide nanocubes with highly interconnected-pore architecture as an efficient polysulfide mediator for lithium–sulfur batteries. *ACS Nano* **13**, 4731–4741 (2019).

44. Kim, M.-S. et al. Facile and scalable fabrication of high-energy-density sulfur cathodes for pragmatic lithium–sulfur batteries. *J. Power Sources* **422**, 104–112 (2019).

45. Li, Y. et al. Two birds with one stone: interfacial engineering of multifunctional Janus separator for lithium–sulfur batteries. *Adv. Mater.* **34**, 2107638 (2022).

46. Luo, L., Chung, S. H., Yaghoobnejad Asl, H. & Manthiram, A. Long-life lithium–sulfur batteries with a bifunctional cathode substrate configured with boron carbide nanowires. *Adv. Mater.* **30**, 1804149 (2018).

47. Qie, L. & Manthiram, A. High-energy-density lithium–sulfur batteries based on blade-cast pure sulfur electrodes. *ACS Energy Lett.* **1**, 46–51 (2016).

48. Fang, Z. et al. Mesoporous carbon nanotube aerogel–sulfur cathodes: A strategy to achieve ultrahigh areal capacity for lithium–sulfur batteries via capillary action. *Carbon* **166**, 183–192 (2020).

49. Hu, S. et al. Ionic-liquid-assisted synthesis of FeSe–MnSe heterointerfaces with abundant Se vacancies embedded in N, B co-doped hollow carbon microspheres for accelerating the sulfur reduction reaction. *Adv. Mater.* **34**, 2204147 (2022).

50. Xue, W. et al. Intercalation-conversion hybrid cathodes enabling Li-S full-cell architectures with jointly superior gravimetric and volumetric energy densities. *Nat. Energy* **4**, 374–382 (2019).

51. Huang, Y. et al. Sulfur cathodes with self-organized cellulose nanofibers in stable Ah-level, >300 Wh kg^{-1} lithium–sulfur cells. *Adv. Energy Mater.* **12**, 2202474 (2022).

52. Zhao, C.-X. et al. Semi-immobilized molecular electrocatalysts for high-performance lithium–sulfur batteries. *J. Am. Chem. Soc.* **143**, 19865–19872 (2021).

53. Zhao, C. et al. A high-energy and long-cycling lithium–sulfur pouch cell via a macroporous catalytic cathode with double-end binding sites. *Nat. Nanotechnol.* **16**, 166–173, (2021).

54. Zhao, M. et al. Redox co-mediation with organopolysulfides in working lithium–sulfur batteries. *Chem* **6**, 3297–3311 (2020).

55. Song, Y.-W. et al. Cationic lithium polysulfides in lithium–sulfur batteries. *Chem* **8**, 3031–3050 (2022).

56. Chen, J. et al. Improving lithium–sulfur battery performance under lean electrolyte through nanoscale confinement in soft swellable gels. *Nano Lett.* **17**, 3061–3067 (2017).

57. Niu, C. et al. High-energy lithium metal pouch cells with limited anode swelling and long stable cycles. *Nat. Energy* **4**, 551–559 (2019).

58. Sander, J., Erb, R. M., Li, L., Gurijala, A. & Chiang, Y.-M. High-performance battery electrodes via magnetic templating. *Nat. Energy* **1**, 16099 (2016).

59. Kang, N. et al. Cathode porosity is a missing key parameter to optimize lithium–sulfur battery energy density. *Nat. Commun.* **10**, 4597 (2019).

60. Gao, Y. et al. Low-temperature and high-rate-charging lithium metal batteries enabled by an electrochemically active monolayer-regulated interface. *Nat. Energy* **5**, 534–542 (2020).

61. Kim, M. S. et al. Langmuir–Blodgett artificial solid-electrolyte interphases for practical lithium metal batteries. *Nat. Energy* **3**, 889–898 (2018).

62. Liang, X. et al. A facile surface chemistry route to a stabilized lithium metal anode. *Nat. Energy* **2**, 17119 (2017).

63. Cha, E. et al. 2D MoS_2 as an efficient protective layer for lithium metal anodes in high-performance Li–S batteries. *Nat. Nanotechnol.* **13**, 337–344 (2018).

64. He, X. et al. The passivity of lithium electrodes in liquid electrolytes for secondary batteries. *Nat. Rev. Mater.* **6**, 1036–1052 (2021).

65. Wang, Q. et al. Interface chemistry of an amide electrolyte for highly reversible lithium metal batteries. *Nat. Commun.* **11**, 4188 (2020).

66. Holoubek, J. et al. Tailoring electrolyte solvation for Li metal batteries cycled at ultra-low temperature. *Nat. Energy* **6**, 303–313 (2021).

67. Ko, S. et al. Electrode potential influences the reversibility of lithium metal anodes. *Nat. Energy* **7**, 1217–1224 (2022).

68. Yin, Y. J. et al. Fire-extinguishing, recyclable liquefied-gas electrolytes for temperature-resilient lithium metal batteries. *Nat. Energy* **7**, 548–559 (2022).

69. Kresse, G. & Furthmüller, J. Efficiency of ab-initio total energy calculations for metals and semiconductors using a plane–wave basis set. *Comput. Mater. Sci.* **6**, 15–50 (1996).

70. Kresse, G. & Furthmüller, J. Efficient iterative schemes for ab initio total-energy calculations using a plane–wave basis set. *Phys. Rev. B* **54**, 11169–11186 (1996).

71. Perdew, J. P., Burke, K. & Ernzerhof, M. Generalized gradient approximation made simple. *Phys. Rev. Lett.* **77**, 3865–3868 (1996).

72. Blöchl, P. E. Projector augmented-wave method. *Phys. Rev. B* **50**, 17953–17979 (1994).

73. Kresse, G. & Joubert, D. From ultrasoft pseudopotentials to the projector augmented-wave method. *Phys. Rev. B* **59**, 1758–1775 (1999).

74. Dudarev, S. L., Botton, G. A., Savrasov, S. Y., Humphreys, C. J. & Sutton, A. P. Electron-energy-loss spectra and the structural stability of nickel oxide: an LSDA+U study. *Phys. Rev. B* **57**, 1505–1509 (1998).

75. Wang, L., Maxisch, T. & Ceder, G. Oxidation energies of transition-metal oxides within the GGA+U framework. *Phys. Rev. B* **73**, 195107 (2006).

76. Ren, Y. X., Zhao, T. S., Liu, M., Tan, P. & Zeng, Y. K. Modeling of lithium–sulfur batteries incorporating the effect of Li_2S precipitation. *J. Power Sources* **336**, 115–125 (2016).

77. Zhang, T., Marinescu, M., Walus, S. & Offer, G. J. Modelling transport-limited discharge capacity of lithium–sulfur cells. *Electrochim. Acta* **219**, 502–508 (2016).

Acknowledgements

Author contributions

G.Z. and Z.H. conceived the idea and designed the project. G.Z. supervised the experiments and edited the paper. Z.H., R.G., Y.J. and Z.L. performed the catalyst synthesis and tested the catalysts. T.W. contributed to the DFT calculations parts. S.T. and J.Z. contributed to the Pearson correlation and machine-learning analysis. M.Z. conducted the COMSOL simulations. All authors analysed the data and discussed the results.

Competing interests

The authors declare no competing interests.

Additional information

Supplementary information The online version contains supplementary material available at https://doi.org/10.1038/s41929-023-01041-z.

Correspondence and requests for materials should be addressed to Guangmin Zhou.

Peer review information *Nature Catalysis* thanks Jinjin Li and the other, anonymous, reviewer(s) for their contribution to the peer review of this work.

Reprints and permissions information is available at www.nature.com/reprints.

Publisher's note Springer Nature remains neutral with regard to jurisdictional claims in published maps and institutional affiliations.